5. FLOW AND TRANSPORT MODELING RESULTS

For the primary flow and transport modeling for the sites, using the significant uncertain parameters identified in the parametric uncertainty analysis (K, *Rech*, and θ), the same model meshes employed in the parametric uncertainty analysis of Section 4 are used. Again, these meshes differ from those used in the calibration (Figure 2.8) because the chimneys created by collapse into the nuclear cavities are included. These features were not used during calibration because the calibration data for each site were obtained prior to each test. It is assumed that the hydrologic impact of the chimneys is an enhancement in vertical conductivity; as a result, no anisotropy is applied in those model cells, resulting in an increase in vertical hydrologic conductivity of ten times over the rest of the domain. Figure 5.1 shows the upper left portion of the simulation domain for the three tests with the chimney location highlighted.

5.1 Milrow Flow and Transport Results

Three new random distributions are generated for the conductivity, recharge and fracture porosity. The same distributions generated in the first stage are not used for two reasons. First, the new distributions have 500 values of each parameter as opposed to only 100 values in the first stage. Second, an upper and a lower limit for the recharge-conductivity ratio are specified to ensure that the transition zone is within the depths identified by the chloride data. This is intended to reduce the uncertainty in the location of the transition zone and to guarantee a converging solution with no boundary effects. Therefore, 500 random K values and a similar number for *Rech* are generated with no correlation among the generated values. The cases that satisfy the condition $0.0013 \leq Rech/K \leq 0.0347$ are then selected, which yields 300 realizations of the random values. These limits are chosen based on the individual results of the first stage and the location of the transition zone relative to the chloride concentration data. The minimum, mean and maximum values of K are 2.2×10^{-3}, 1.69×10^{-2}, and 6.24×10^{-2} m/day, respectively. For the recharge, these limits are 0.319, 2.066, and 6.65 cm/year, respectively. Independently of these values, 300 random porosity values with a minimum of 1.057×10^{-5}, a mean of 4.4×10^{-4}, and a maximum of 6.2×10^{-3} are generated. Figure 5.2 displays the histograms of these three distributions. In comparing these distributions to those used in stage one, it is found that recharge and conductivity distributions have higher means in this stage. Porosity distribution on the other hand shows a lower mean than in the first modeling stage, which is toward the conservative side.

It is interesting to compare the recharge-conductivity ratio and the conductivity-porosity ratio for the new distributions to the base-case values. Recall that in the base case, $K = 6.773 \times 10^{-3}$ m/day, *Rech*$= 1.125 \times 10^{-4}$ cm/year, and $\theta = 5.0 \times 10^{-4}$. The plots in Figure 5.3 illustrate how the two ratios (*Rech*/K and K/θ) vary among the 300 realizations around the base-case ratios. As can be seen in the figure, *Rech*/K varies from a minimum that is four times smaller than the base case to a maximum that is six times larger. More realizations lie below the base-case line than above it, which indicates some skewness towards the high conductivity values. The conductivity-porosity ratio varies from ten times smaller to about 160 times larger than the base-case value. As will be seen later, this distribution represents conservative *K-Rech* combinations since the critical combinations are those having a large recharge-conducitivty ratio. The figure also shows that more realizations lie in the high K/low θ region

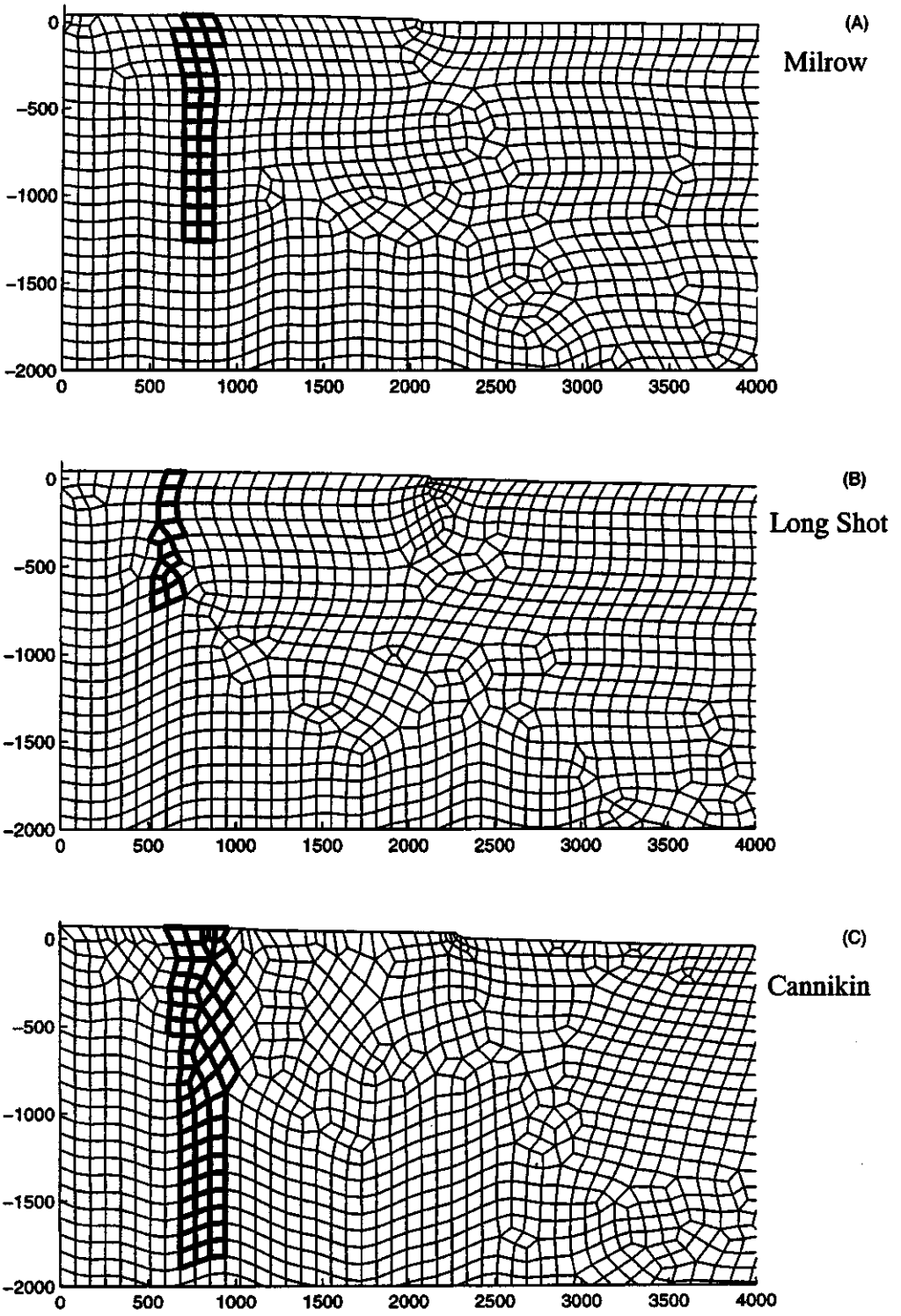

Figure 5.1. Expanded view of the upper left portion of each model domain, showing the nuclear chimney included in the flow and transport simulations.

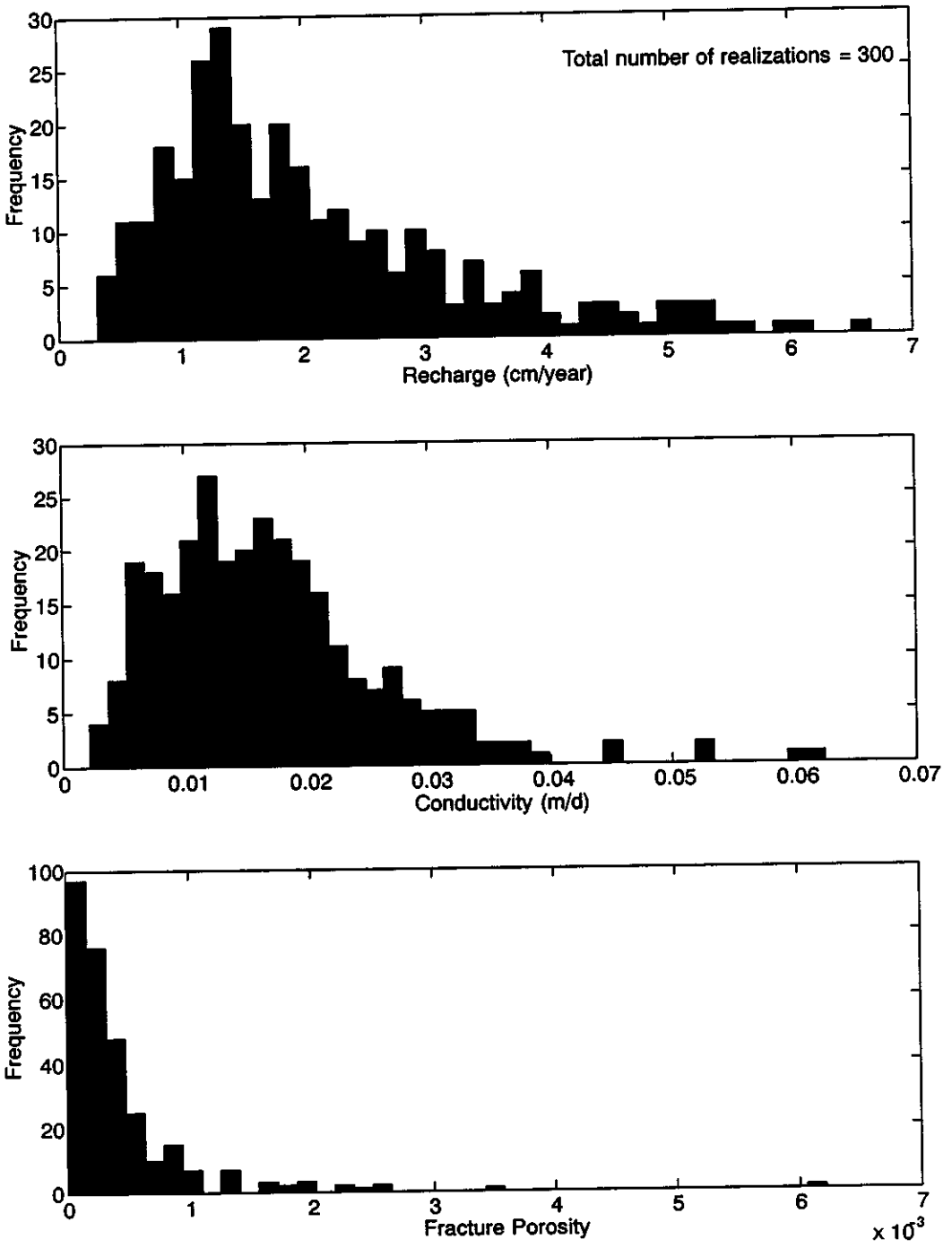

Figure 5.2. Randomly generated distributions for *Rech*, *K*, and θ in the second modeling stage for Milrow.

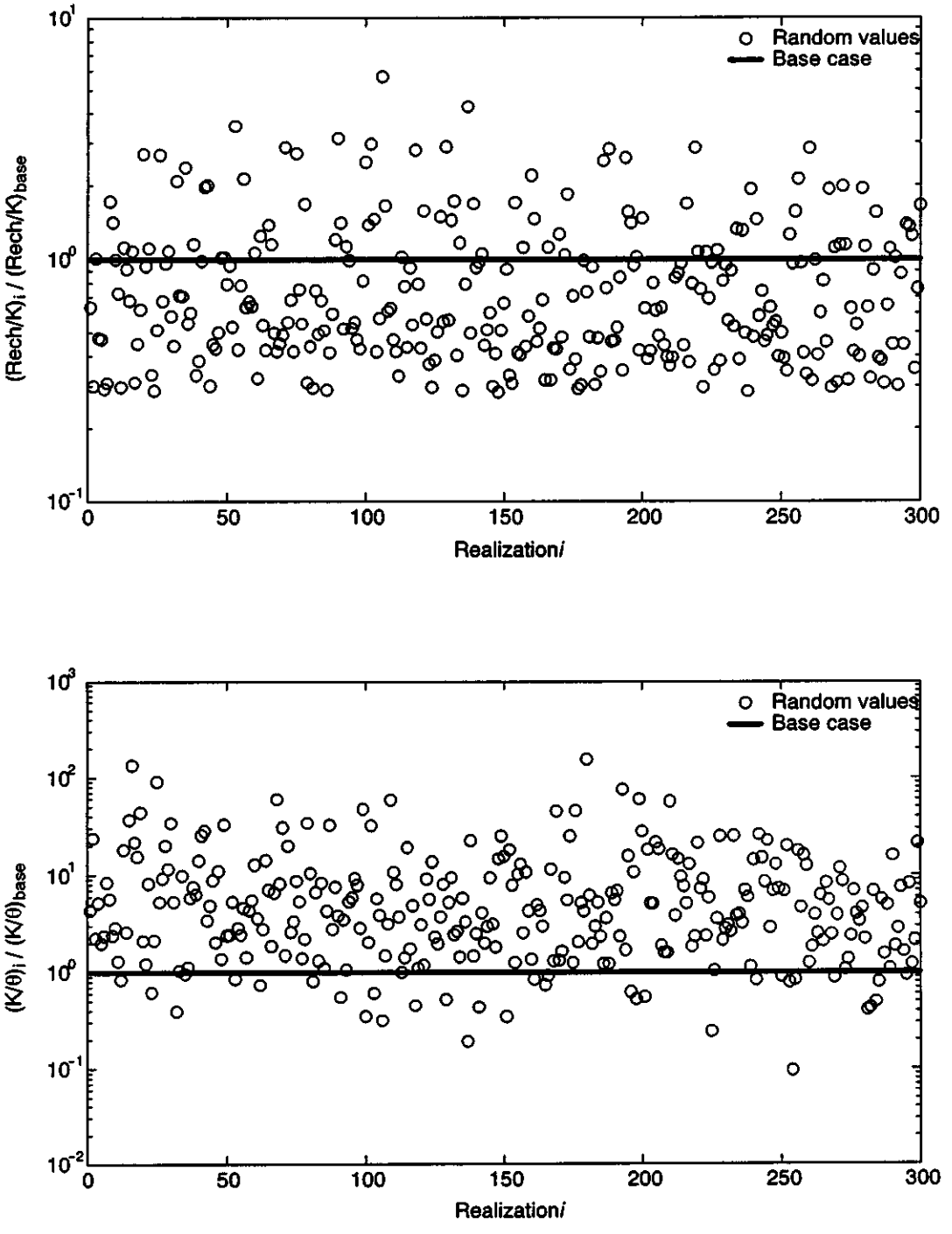

Figure 5.3. Comparison of the randomly generated recharge-conductivity ratio and conductivity-porosity ratio in relation to the Milrow base-case values.

than in the opposite region. This is again on the conservative side, as more realizations are produced with very high velocities than with low velocities.

The solution of the flow problem in this stage is performed similarly to the first stage, with the parameters summarized in Table 5.1. FEFLOW is used to solve the density-driven flow problem for 300 realizations with the recharge, conductivity, and porosity values already generated. Macrodispersivity values are fixed at 100 m and 10 m in the longitudinal and transverse directions, respectively. Domain geometry and boundary conditions remain unchanged. To assess the choice of the combined random values used in this analysis, the results of these realizations are analyzed at the UAe-2 location. Figure 5.4 displays the simulated concentration and head profiles in UAe-2 in terms of the mean of the 300 realizations, the mean ± one standard deviation, the base-case result and the measured data. The first observation in this figure is that the mean of the MC realizations is closer to the data points than any of the individual cases investigated in the first stage (*e.g.*, Figure 4.3 through Figure 4.6). Furthermore, the one standard deviation confidence interval encompasses all the data points for the chloride concentration. The confidence interval also encompasses all head data, although the mean of the MC runs gives lower heads than the measurements. The overall result is that the ranges of variabilities considered encounter a large number of possible combinations that cover a wide range of uncertainty in the flow parameters.

Table 5.1. Parameter range for Milrow simulations.

Parameter	Minimum	Mean	Maximum	σ	Distribution
K	2.2×10^{-3}	1.69×10^{-2}	6.24×10^{-2}	9.3×10^{-3}	~ lognormal
Rech	0.319	2.066	6.65	1.24	~ lognormal
θ	1.057×10^{-5}	4.4×10^{-4}	6.2×10^{-3}	5.92×10^{-4}	~ lognormal
A_L	-	100	-	-	-
A_T	-	10	-	-	-
α_L	-	5.0	-	-	-
α_T	-	0.5	-	-	-
κ	-	0.434	-	-	-
K_g	-	1.26×10^{-7}	-	-	-

Radionuclide transport simulations are also performed in a manner similar to the first stage described in Section 4. All transport parameters are kept constant in all realizations. Glass dissolution rate, k_g, is taken as 1.26×10^{-7} day^{-1}, local dispersivities are fixed at 5.0 and 0.5 m, and the matrix diffusion parameter is assigned a value of 0.434 (consistent with a θ_m of 0.12, a b of 5.0 $\times 10^{-4}$ m and a D^*_m of 3.28×10^{-6} m^2/day).

The particle-tracking transport simulations are performed for six cases with different release ratios and retardation behavior. The 24 radionuclides (parents and daughters) chosen for investigation are grouped into six solute classes based on their ratio of hydraulic release to geochemical release and retardation factor, and are listed in Table 5.2. The transport of the radionuclides in each solute class is simulated as a group, followed by application of the radioactive

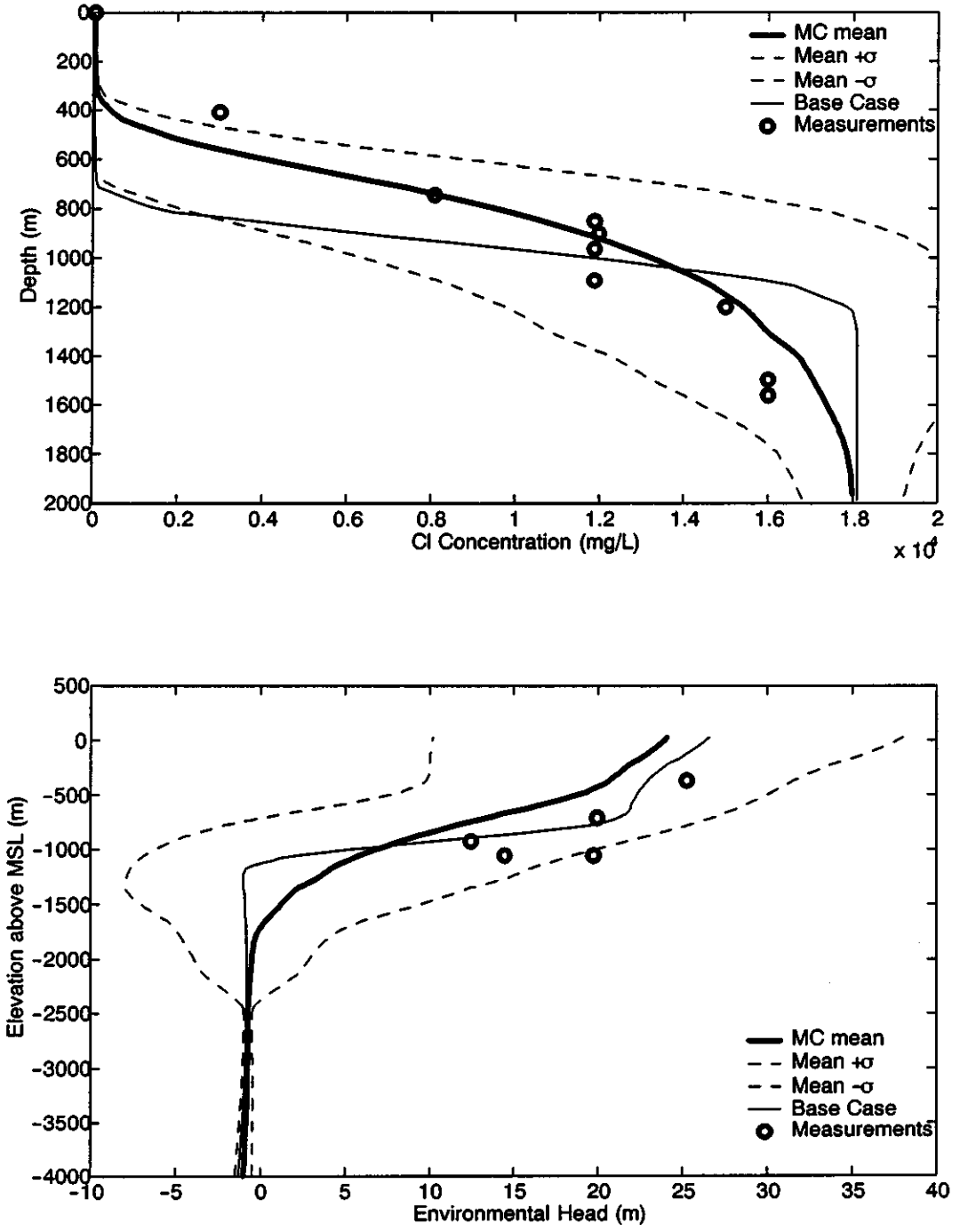

Figure 5.4. Sensitivity of UAe-2 concentrations and heads to the combined uncertainties of *Rech, K* and θ in the second Milrow modeling stage.

decay rate appropriate to each individual radionuclide. The total simulation time and the time step are scaled for each class using the appropriate retardation factor in such a way that the same average length is traversed by particles as for the cases with no retardation. Among the six cases, only Case 6 has a retardation factor of about 1.8 in the fractured system, and thus the simulation time and the time step are scaled with a factor of 2.0. The results of Monte Carlo simulations are presented in terms of the mean and standard deviation of the total solute flux, $Q(t)$, the point solute flux, $q(x, t)$, and the flux-averaged concentration, $C(x, t)$, where x is the distance from the groundwater divide (island center) to the bathymetric segment at which q and C are computed.

Table 5.2. Values of Parameters Specific to Individual Solute Classes.

Parameter	Case 1	Case 2	Case 3	Case 4	Case 5	Case 6
Total Time (years)	2191	2191	2191	2191	2191	4382
Time Step, Δt (days)	100	100	100	100	100	200
Release Ratio (%), Hydraulic Release / Geochemical Release	100/0	50/50	60/40	20/80	80/20	5/95
Retardation Factor	1	1	1	1	1	1.8
Geochemical Release Coefficient kg (day^{-1})	NA	1.26×10^{-7}	1.26×10^{-7}	1.26×10^{-7}	1.26×10^{-7}	1.26×10^{-7}

5.1.1 Undecayed Breakthrough Curves

The effects of the hydraulic/geochemical release ratio, the retardation, and the glass dissolution coefficient of the six solute classes are most effectively examined without the effects of radioactive decay. This is because the widely differing decay rates of the individual radionuclides conceal the general release and retardation behavior. It is also of interest to present the undecayed breakthrough curves with and without the inclusion of matrix diffusion to capture the effect of the matrix diffusion process.

Figure 5.5 (top) shows the undecayed breakthrough curves for the first solute class (100 percent hydraulic release) with and without matrix diffusion. Without matrix diffusion, a very early breakthrough is observed where the first mass arrival occurs at about five years after the test. As will be shown later, this early breakthrough is mainly controlled by a few realizations that have very high velocities (due to certain combinations of $Rech$, K and θ). When adding matrix diffusion ($\kappa = 0.0434$ and 0.434), a significant reduction in the mass flux values is obtained and a significant delay in mass arrival time. A typical feature of the matrix diffusion effect is to delay the arrival of mass to the breakthrough boundary, reduce the peak and induce a tailing effect. The shape and length of the tailing effect depends on the parameters governing the diffusion into the rock matrix, which are lumped into the κ parameter. The effect of κ will be addressed in the sensitivity analysis (Section 6.1.2).

The lower plot of Figure 5.5 shows the undecayed mass flux for the six solute classes with $\kappa = 0.434$. It is clear that the shapes of the first five curves are similar with the difference caused

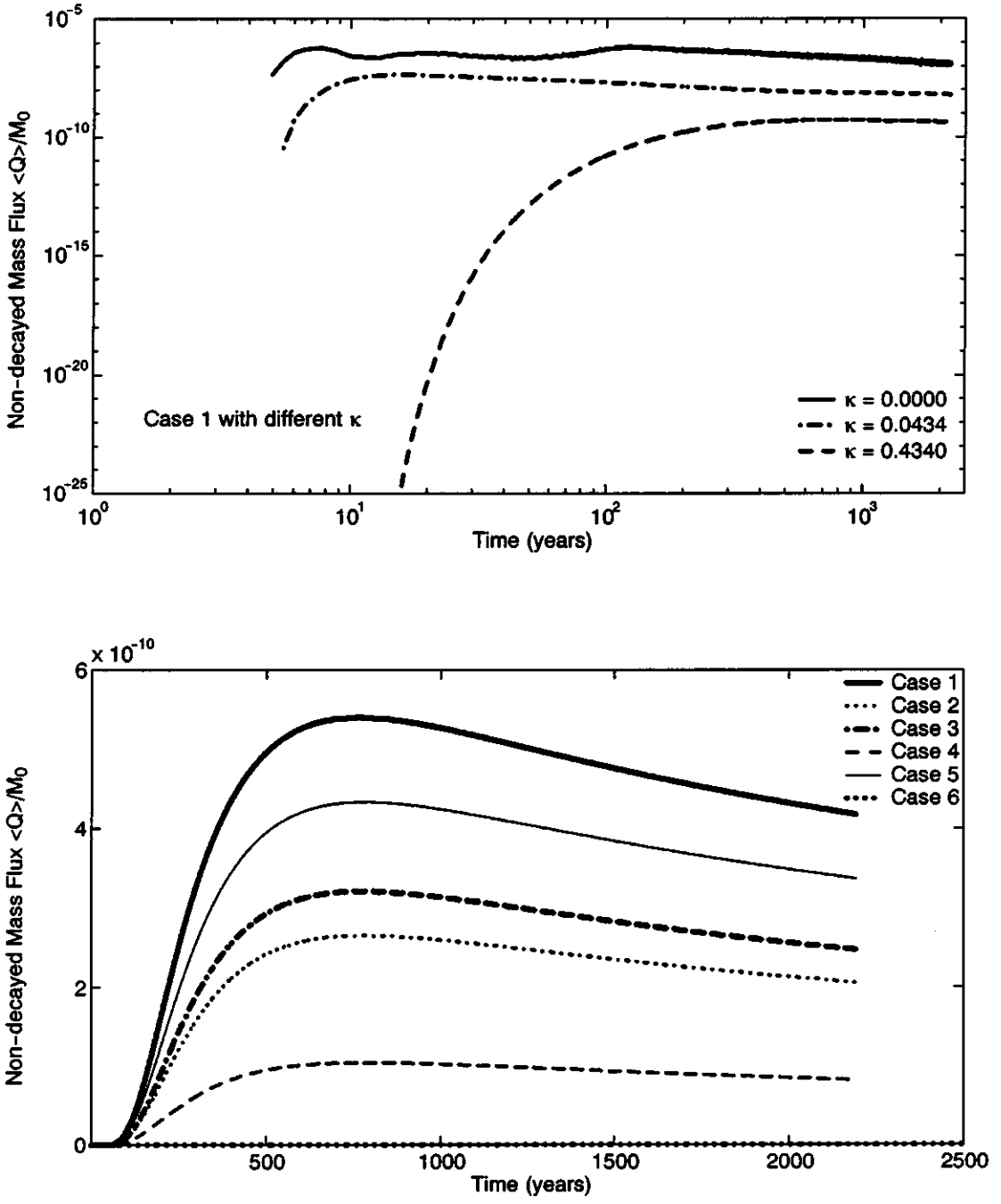

Figure 5.5. Undecayed Milrow breakthrough curves for the first solute class with different matrix diffusion strengths (top) and for the six solute classes with $\kappa = 0.434$ (bottom).

by the differing hydraulic/geochemical release ratio. Case 6 shows no significant mass flux due to the large retardation into the rock matrix. As Table 5.2 indicates, the first five classes differ only in the hydraulic/geochemical release ratio. This ratio has a major effect on the resulting mass flux and breakthrough curves because of the fact that travel time to the seafloor is much smaller than the time scale within which all glass mass is dissolved and released to the domain. That is to say that the mass flux within the short time scale of 2,200 years is mainly caused by the portion of mass subjected to hydraulic release that is assumed to occur instantaneously.

To shed more light on the early mass arrival to the seafloor and the individual realizations' results, the conservative breakthrough results (without matrix diffusion) are studied for Case 1. The 300 realizations are analyzed in terms of the percentage of mass that breaks through within 2,200 years, the first arrival time, the duration of breakthrough, the location of the plume edges with respect to the bathymetric profile and the depths below MSL where breakthrough occurs. Figure 5.6 shows the distribution of the mass percentage that reaches the seafloor within the 2,200-year time frame. About 100 realizations show less than 1 percent of the total mass reaching the breakthrough boundary. Out of these realizations, 25 do not show any mass breakthrough. A total number of about 150 realizations have less than 5 percent of the total mass out within that time frame, 165 have less than 10 percent of the mass out and only about 13 realizations have above 90 percent of the mass out. It should be mentioned, however, that those realizations showing a very small percentage of mass breaking through may in fact contribute more to the peak mass flux and the early arrival of mass. That is to say that a realization with only 5 percent of mass out may contribute significantly to the peak flux and concentration if this portion of the mass arrives very early at the boundary.

To explain why some realizations do not show any breakthrough within the selected time frame, we plot in Figure 5.7 particle trajectories (advective-dispersive) in two realizations with the top plot showing a no-mass-breakthrough realization and the bottom one showing a realization with >90 percent mass breakthrough. The trajectories shown are for a particle released at the lower left corner of the cavity. The figure also shows the velocity field in both cases. Due to the location of the cavity below the transition zone in the first case, most (if not all) particles move either toward the island center or vertically in the chimney before they change direction and move toward the seafloor. In addition to this longer path, the velocities encountered below the transition zone are much smaller than above it, as indicated by the relative sizes of the velocity vectors shown in the figure. The other realization, with the cavity located above the transition zone, shows a direct movement for the same particle from the cavity to the seafloor direction. The different flow patterns in these realizations are dependent upon the random combination of the recharge, conductivity and fracture porosity values, while keeping the cavity and chimney porosity fixed at 0.07. The main difference between the two realizations is that in the first one, the transition zone is shallow due to a small recharge-conductivity ratio ($Rech/K = 2.94 \times 10^{-3}$) and the cavity location is at the lower edge of the transition zone. The other realization is having a much deeper transition zone ($(Rech/K = 7.97 \times 10^{-3}$) and the cavity comes closer to the freshwater zone where velocity pattern is more or less uniformly oriented towards the seafloor.

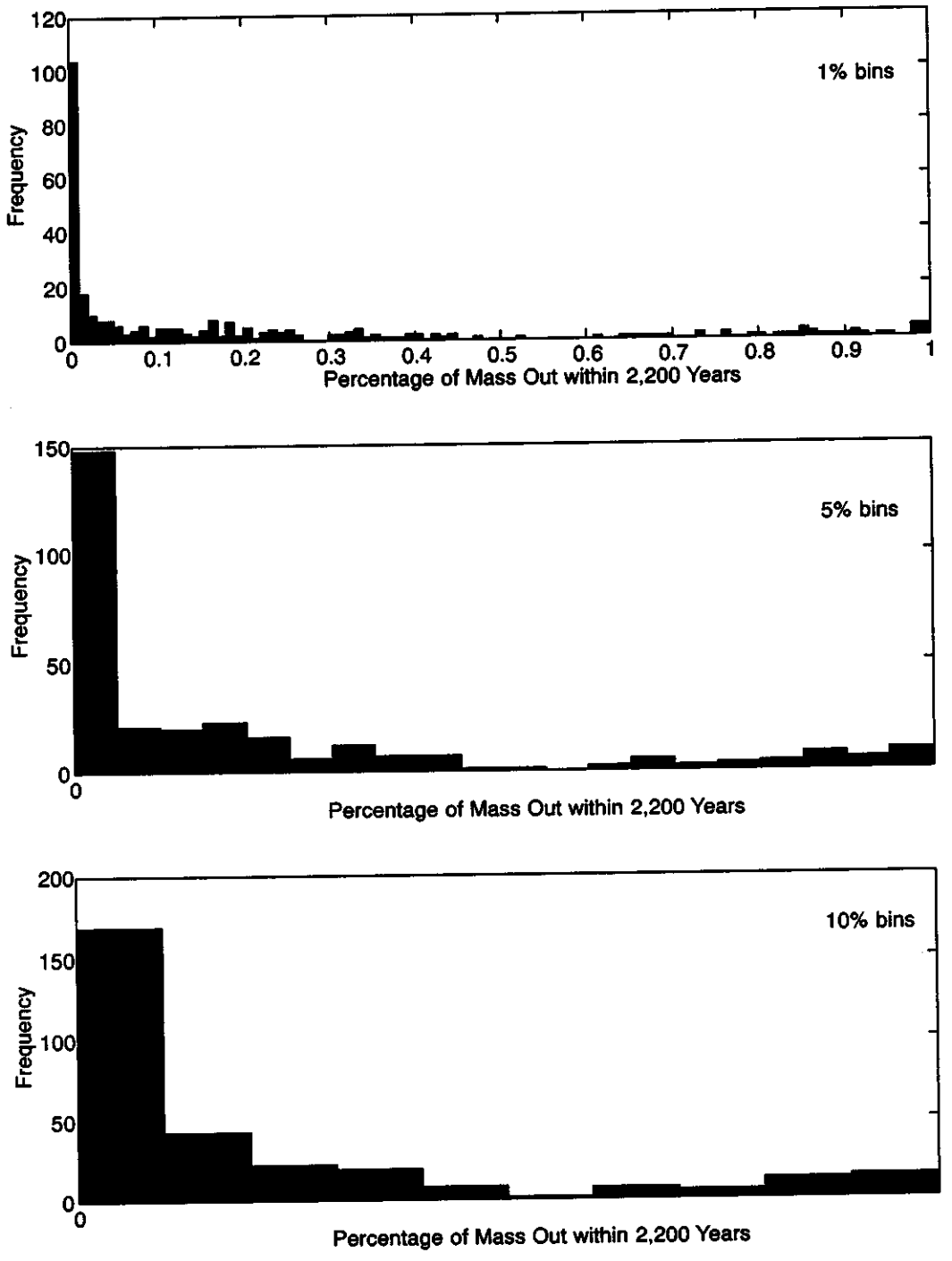

Figure 5.6. Histograms of the percentage of Milrow mass that has broken through within 2,200 years.

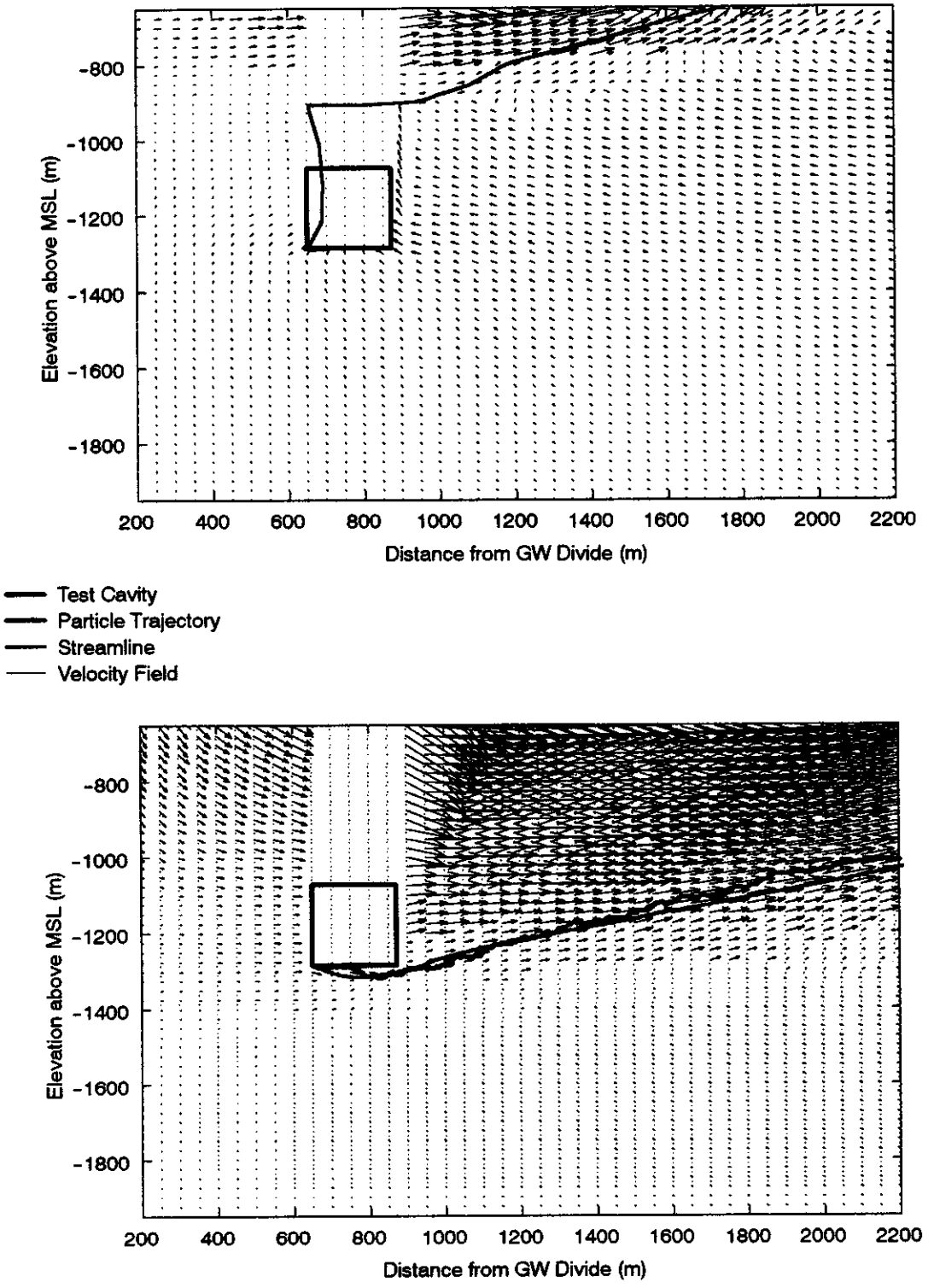

Figure 5.7. Velocity realizations for Milrow showing a circulatory pattern (top) and a non-circulatory pattern (bottom).

To show how the particles travel from the cavity to the seafloor (breakthrough plane), a single realization showing about 100 percent mass breakthrough during the simulation time (2,200 years) is selected for analysis and visualization. The realization is assigned a K value of 4.583×10^{-3} m/d, a *Rech* value of 4.317 cm/year, a porosity value of 1.067×10^{-3}, and a recharge-conductivity ratio of 2.58×10^{-2}. The particles location at different times are reported and used to visualize the plume shape and movement. Figure 5.8 through Figure 5.11 show 12 snapshots of the particles' distribution at different times with the percentage mass reaching the seafloor computed and presented on the figures. No particles reach the seafloor within the first 100 years after the detonation. At 140 years, the leading edge of the plume starts to arrive at the seafloor. Larger numbers of particles arrive between 140 and 180 years, with a total of 1.2 percent of the initial mass reaching the seafloor by 180 years. About 55 percent of the total mass arrives at the seafloor between 200 and 500 years (Figure 5.9), and about an additional 17 percent arrives between 500 and 700 years (Figure 5.10). By 1,000 years after detonation, 90 percent of the mass reaches the seafloor and the rest of the mass arrives very slowly over the remaining 1,200 years of simulation (Figure 5.11).

To continue the analysis of individual realizations, Figure 5.12 presents the distributions of the first arrival time (whether it is for one particle or a thousand particles), the last arrival and the duration of breakthrough. The figure illustrates that about 58 realizations show a first mass arrival less than 60 years. Only a few realizations show a last arrival within the 2,200-year simulation time. This is also evident for the histogram of the breakthrough duration, where only about 20 realizations show ceasing of breakthrough in 500 years or less. This ceasing does not necessarily mean full breakthrough, but means that no particles arrive at the seafloor after the last arrival. Figure 5.13 shows the distribution of the location of the plume edges relative to the groundwater divide and the distribution of the plume width before and after accounting for matrix diffusion. The location of the left (first) edge of the plume is concentrated around 3,000 m from the island centerline, while the right (second) edge of the plume is located around 4,000 m in a large number of realizations. These results indicate that the plume before accounting for matrix diffusion is mainly spread over a length less than one kilometer along the bathymetric profile in most of the realizations. The other quantity that is very essential for risk assessment is the depth below MSL where breakthrough occurs, which is shown in Figure 5.14. This shows that the left edge of the plume exists at a depth of 2 to 10 m, whereas the right edge exists at a depth of 5 to 30 m below MSL. As mentioned earlier, 25 realizations out of 300 did not show any breakthrough within the simulation time of 2,200 years.

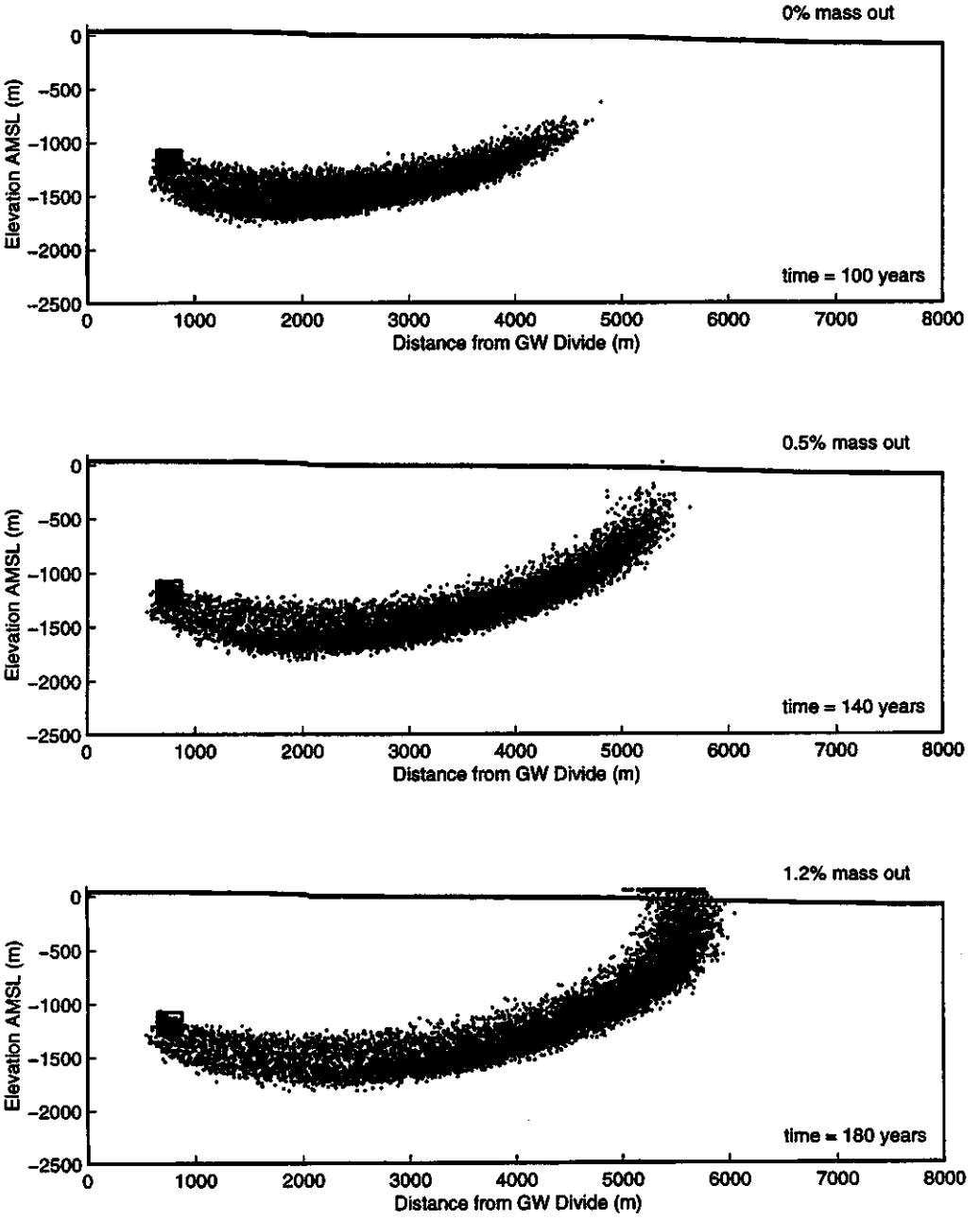

Figure 5.8. Three snapshots of the particle distribution (plume shape) at different times for Milrow.

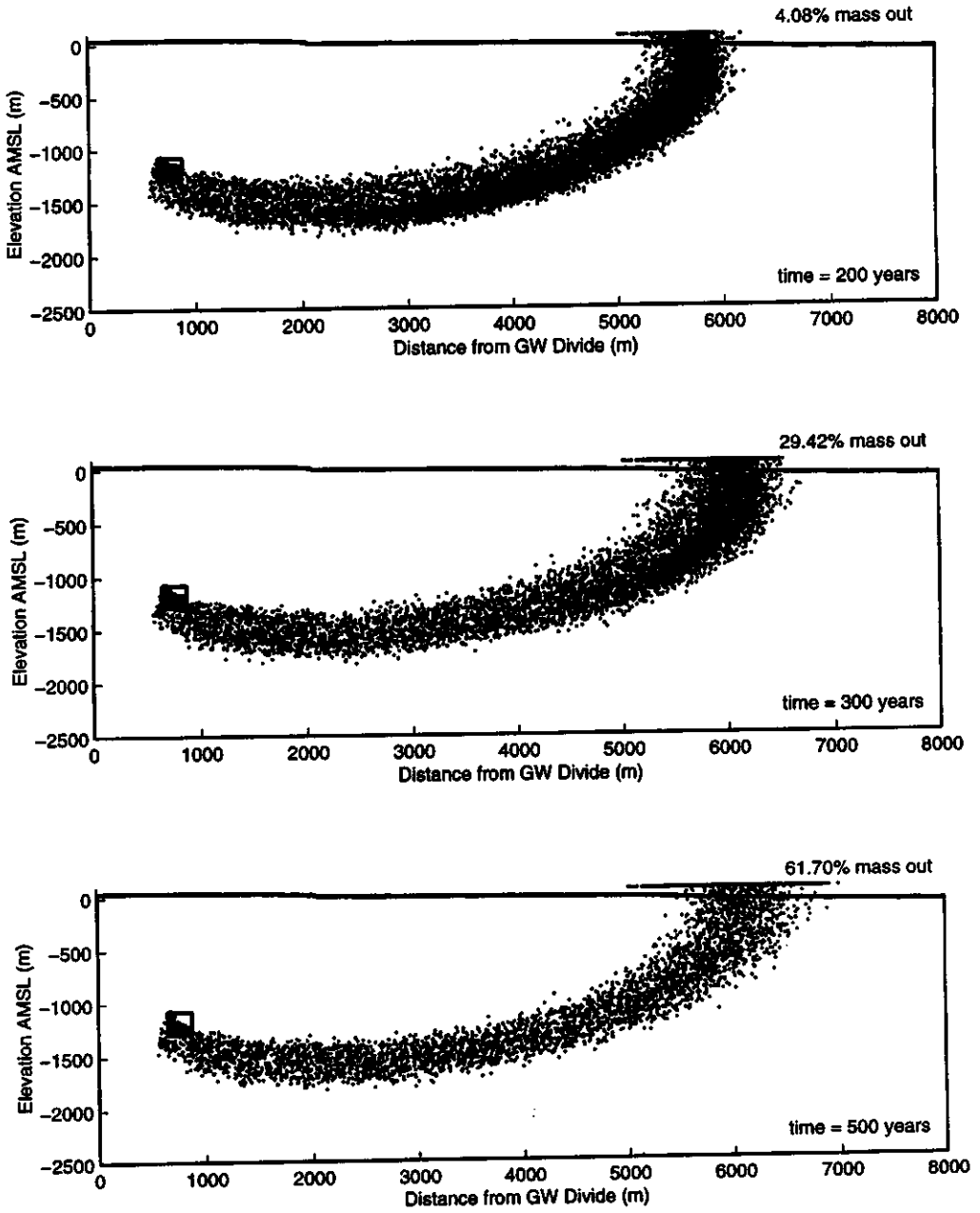

Figure 5.9. Three snapshots of the particle distribution (plume shape) at different times for Milrow.

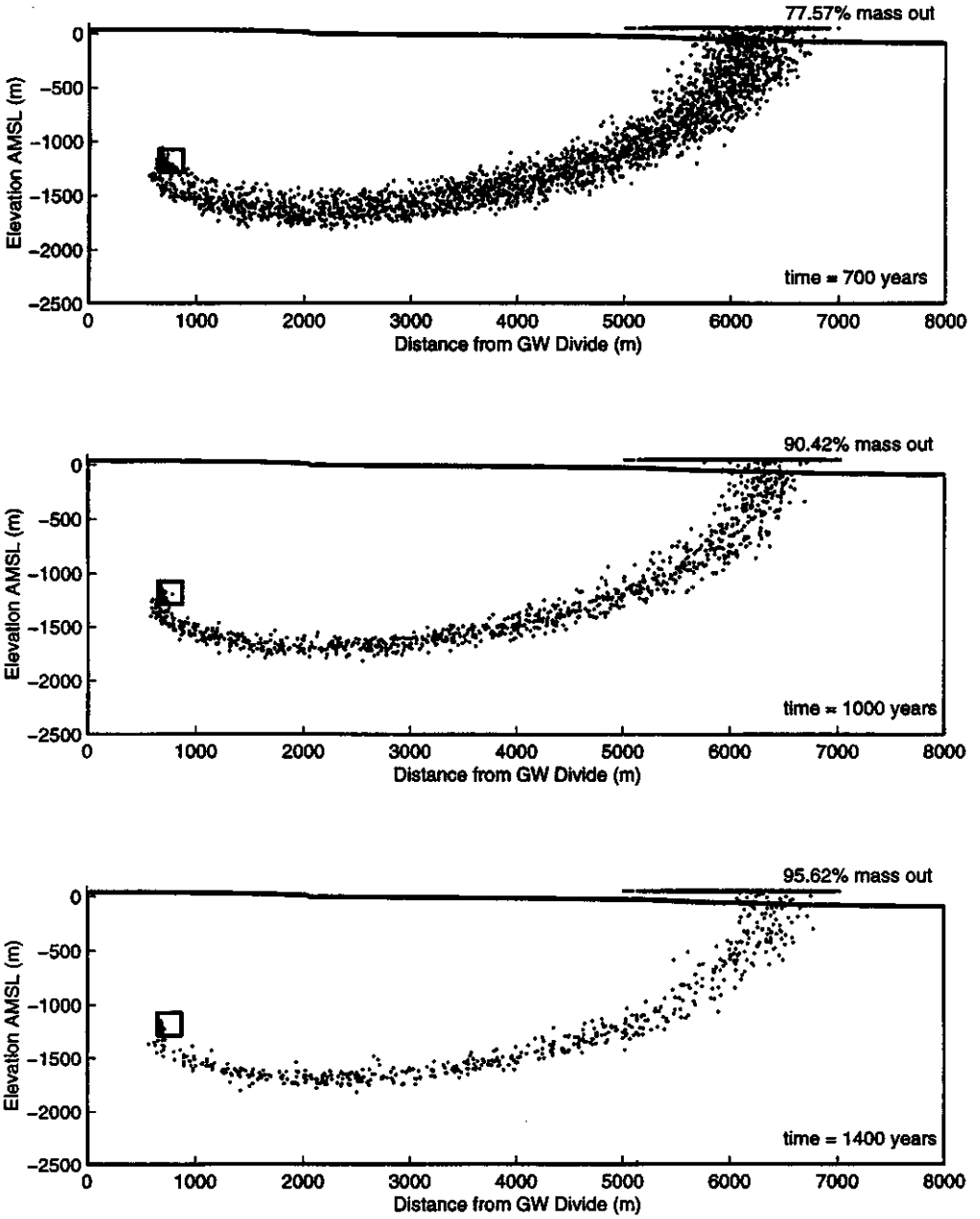

Figure 5.10. Three snapshots of the particle distribution (plume shape) at different times for Milrow.

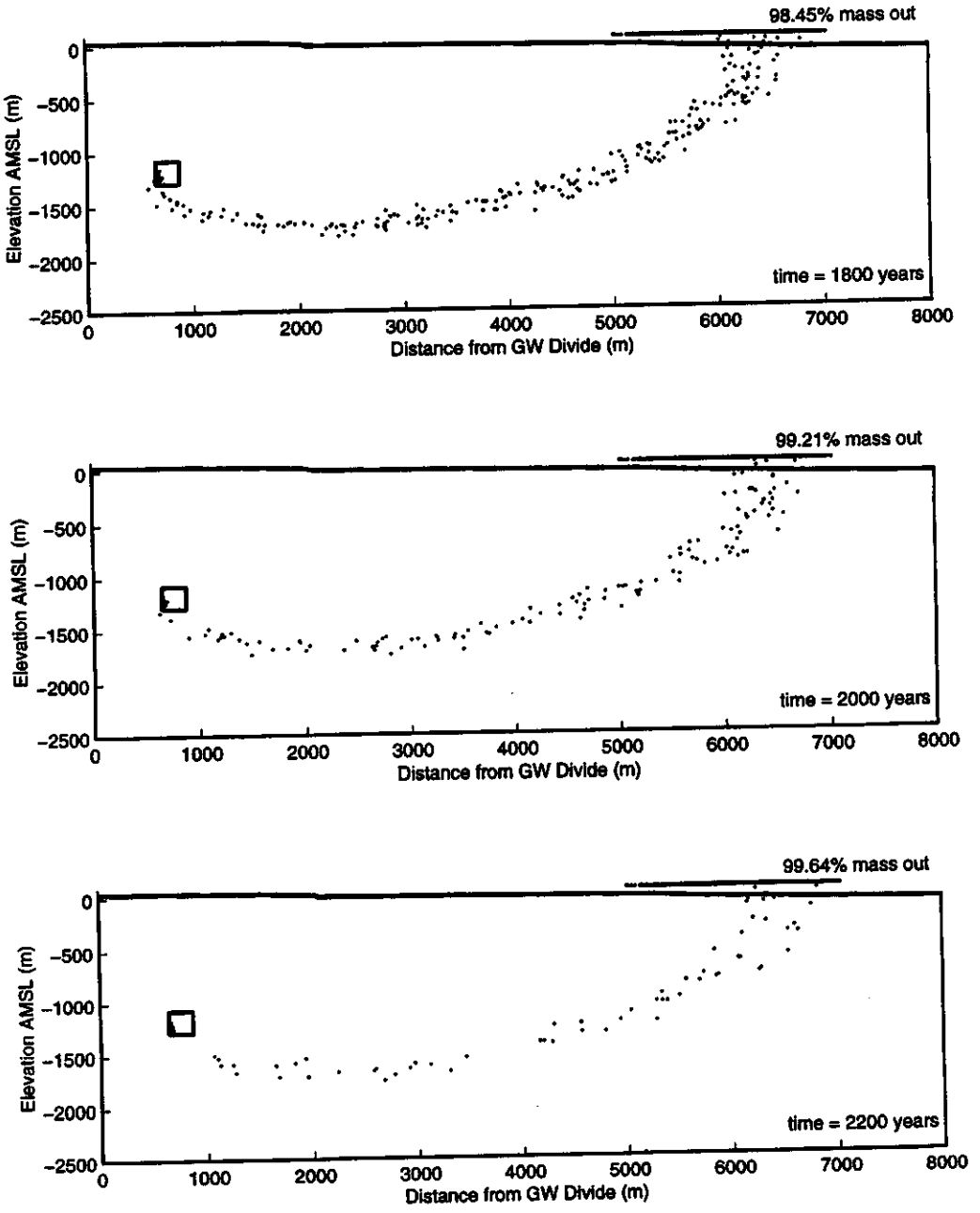

Figure 5.11. Three snapshots of the particle distribution (plume shape) at different times for Milrow.

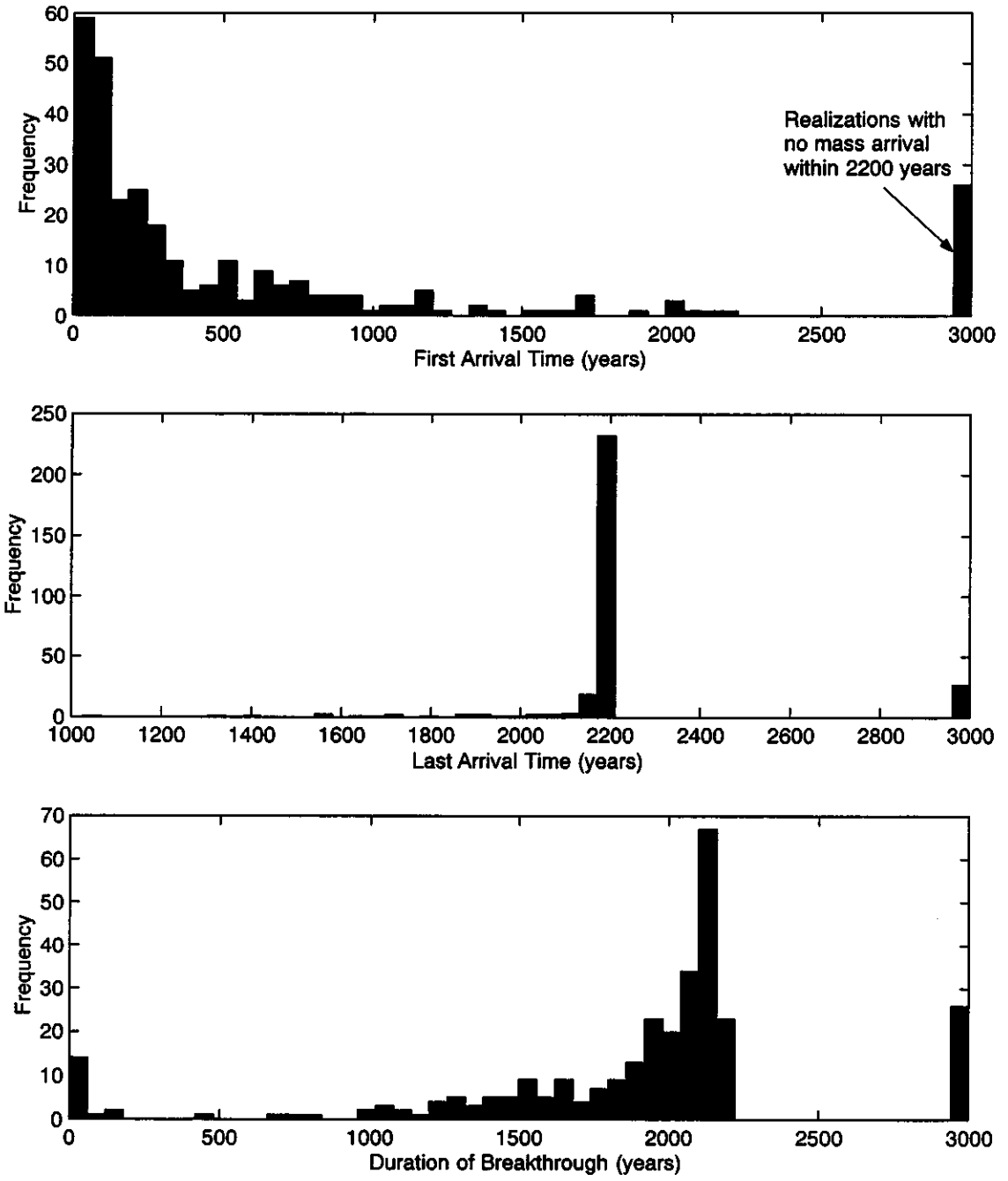

Figure 5.12. Histograms showing the distribution of first arrival time, last arrival time, and duration of breakthrough for Milrow.

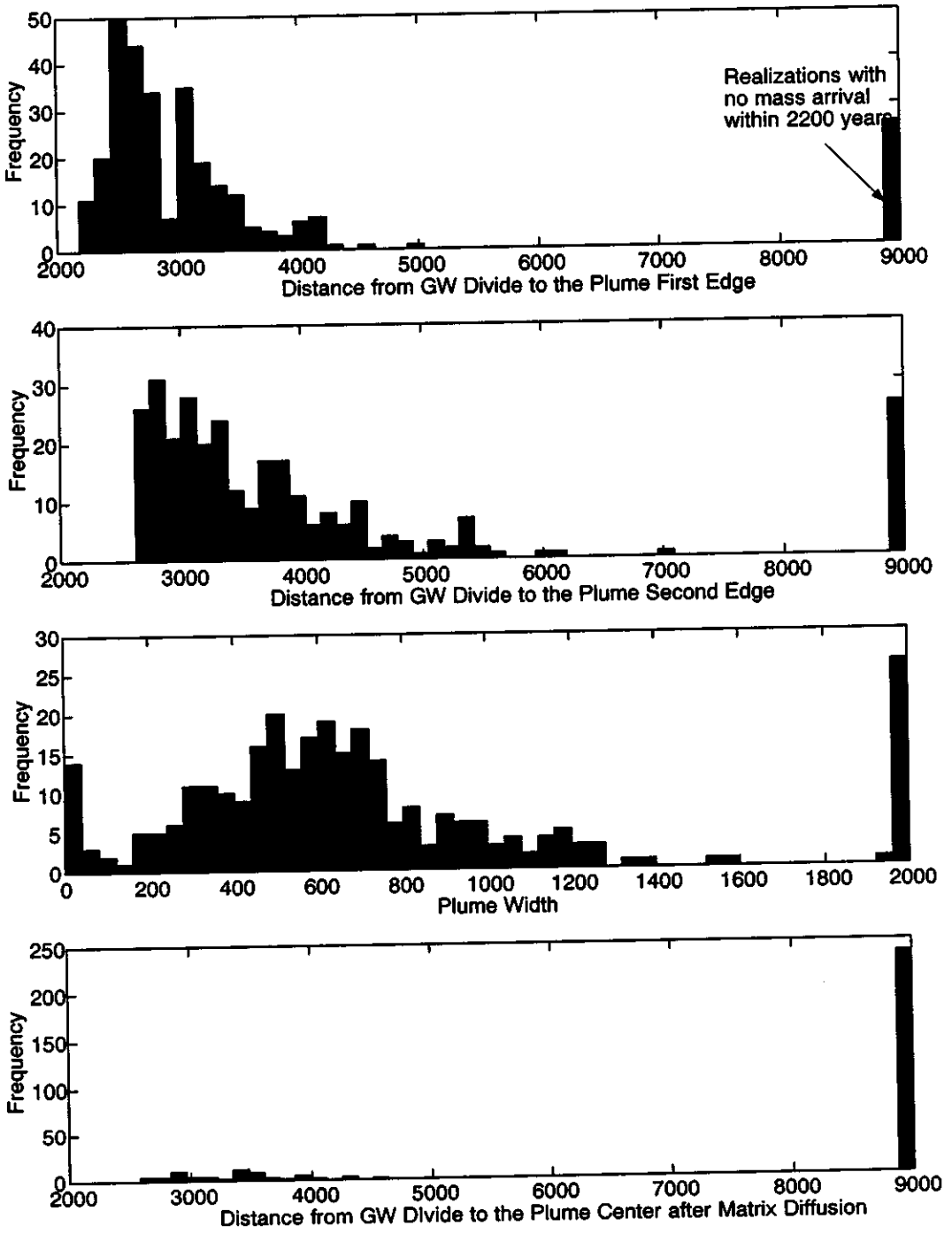

Figure 5.13. Histograms showing the distance from groundwater divide to plume edges and plume width for Milrow.

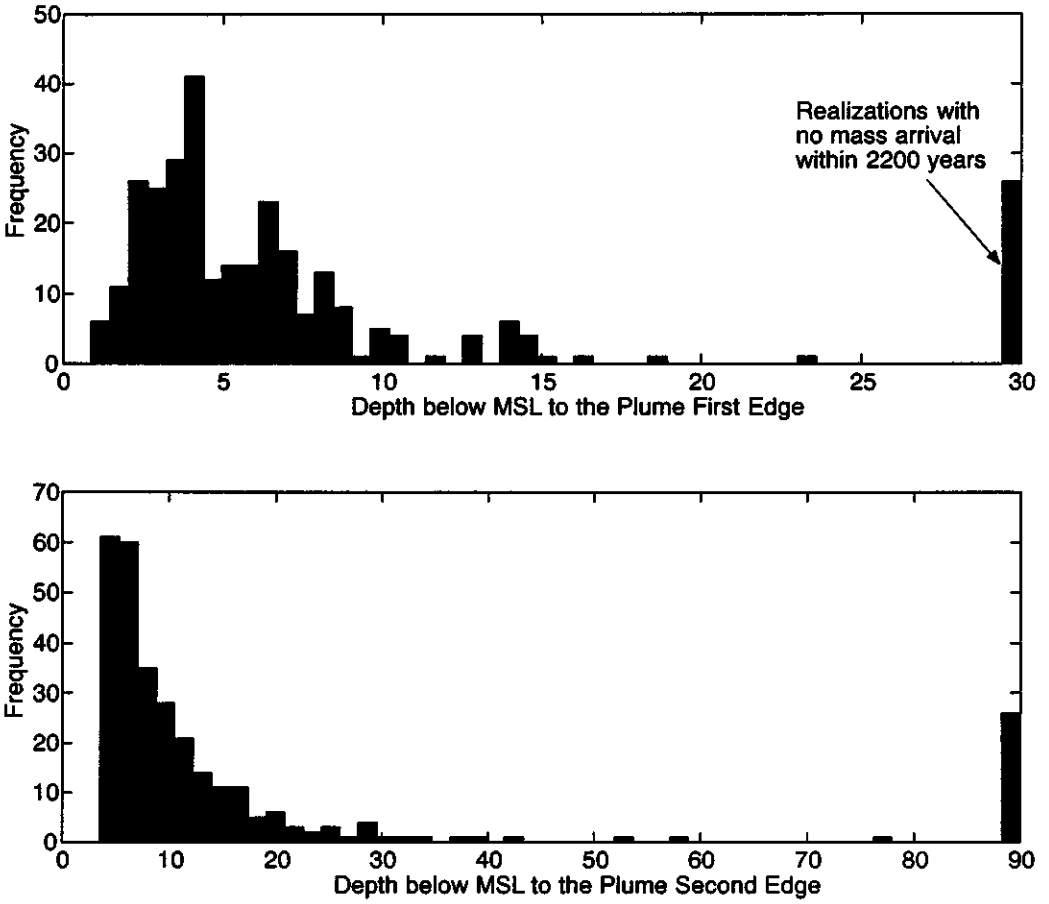

Figure 5.14. Histograms showing the distributions of depths below MSL at which the plume edges discharge to the ocean floor for Milrow.